Journal of
Materials Chemistry C

ROYAL SOCIETY
OF CHEMISTRY

PAPER

View Article Online
View Journal | View Issue

Cite this: *J. Mater. Chem. C*, 2022, **10**, 8728

Paramagnetic supramolecular mesogens: A new paradigm in self-assembled magnetic materials†

Martin Lambov,[a] Philipp Maier,[a] Marcin Jasiński,[b] Jacek Szczytko,[c]
Piotr Kaszyński*[bde] and Matthias Lehmann*[af]

Received 2nd January 2022,
Accepted 29th April 2022

DOI: 10.1039/d2tc00015f

rsc.li/materials-c

Sterically crowded, shape-persistent star mesogens with three oligophenylenevinylene arms provide free space in which Blatter radical guests are incorporated by covalent bonds (esters) or supramolecular interactions (hydrogen bonds). The radical guests transform these compounds to paramagnetic liquid crystalline (LC) materials. The LC molecules are demonstrated to self-assemble into several types of columnar phases, a process that is controlled by the binding mode and the size of the star mesogen cavity. The conjugated scaffold remains stable in the presence of these radicals. Magnetic investigations by means of solid-state VT-EPR and SQUID experiments reveal that these materials are paramagnetic with weak antiferromagnetic interactions. In contrast to the covalent mesogens, the supramolecular systems do not only possess much lower clearing temperatures, but also radical guests exhibit mobility independent of the phase transition leading to soft paramagnetic materials with tunable magnetic properties.

Introduction

In recent decades the design of functional liquid crystals (LCs) has been of great interest owing to their structural control at different levels and the stimuli responsiveness based on their molecular mobility.[1–3] Some of them have been studied intensively for applications in display technologies,[4] organic electronics,[5] optical switching,[6] and stimuli responsive fluorescence applications.[7] There has also been increasing interest in self-organizing paramagnetic molecular materials for technological advances and, in this context, investigation of spininterfaces[8] and spintronic phenomena[9,10] in thin films,[11,12] mesoporous[13,14] and in liquid crystalline materials.[15–18] In particular, the robust 1,4-dihydrobenzo[*e*][1,2,4]triazin-4-yl radical[19] (Blatter[20] radical) has proven to be an attractive building block for the development of novel multi-functional materials[21] for organic batteries,[22] molecular electronics[23,24] and spintronics.[13,25]

Blatter radical derivatives have been designed to self-assemble into photoconductive bent-core[26,27] and discotic[28,29] LCs. The magnetic properties of the columnar LC phases depend on the molecular design of mesogens,[29,30] which, in turn, controls the paramagnetic core overlap and, consequently, the spin–spin exchange interactions in the LC phase.[31] Thus, ''full disc'' Blatter radicals show different magnetic behaviour compared to that of ''half discs''. The ''half disc'' Blatter radicals have also been connected to form isostructural biradicals (''dumbbell'' architecture) or triradicals (''superdisc'' architecture). However, not all of them are LCs.[31]

Recently, the rational design of mesogens providing free space in LC phases for the uptake of guest molecules has been studied as a new method to guide the positional order of functional building blocks in mesophases.[32] It was shown that shape-persistent star mesogens consisting of an alternating substitution pattern around a benzene core with oligo(phenylenevinylene) arms and pyridyl or hydroxyphenyl groups generate pockets, in which guest molecules can be hosted. These endoreceptors are able to accept up to three guests.[33–35] The resulting supramolecular or covalently bonded supermesogens[36] self-assemble in highly ordered double or triple nanosegregated structures.[37,38] These results prompted us to design new supermesogens **1** and **2** (Fig. 1) containing the Blatter radical guests **G1OH** and **G2OH** either covalently or supramolecularly bound to the conjugated sterically crowded star mesogen hosts.

---

[a] *Institute of Organic Chemistry, University of Würzburg, Am Hubland, 97074 Würzburg, Germany*

[b] *Faculty of Chemistry, University of Łódź, Tamka 12, 91-403 Łódź, Poland*

[c] *Institute of Experimental Physics, Faculty of Physics University of Warsaw, Pasteura 5, 02-093 Warsaw, Poland*

[d] *Centre of Molecular and Macromolecular Studies, Polish Academy of Sciences, Sienkiewicza 112, 90363 Łódź, Poland. E-mail: piotrk@cbmm.lodz.pl*

[e] *Organic Materials Research Group, Department of Chemistry, Middle Tennessee State University, Murfreesboro, TN 37132, USA*

[f] *Center for Nanosystems Chemistry and Bavarian Polymer Institute, Theodor-Boveri-Weg 4, 97074 Würzburg, Germany. E-mail: matthias.lehmann@uni-wuerzburg.de*

† Electronic supplementary information (ESI) available: Additional synthetic and compound characterization details, POM data, powder XRD analysis, density measurements, FT-IR and EPR spectra, modeling details and magnetization results. See DOI: **https://doi.org/10.1039/d2tc00015f**

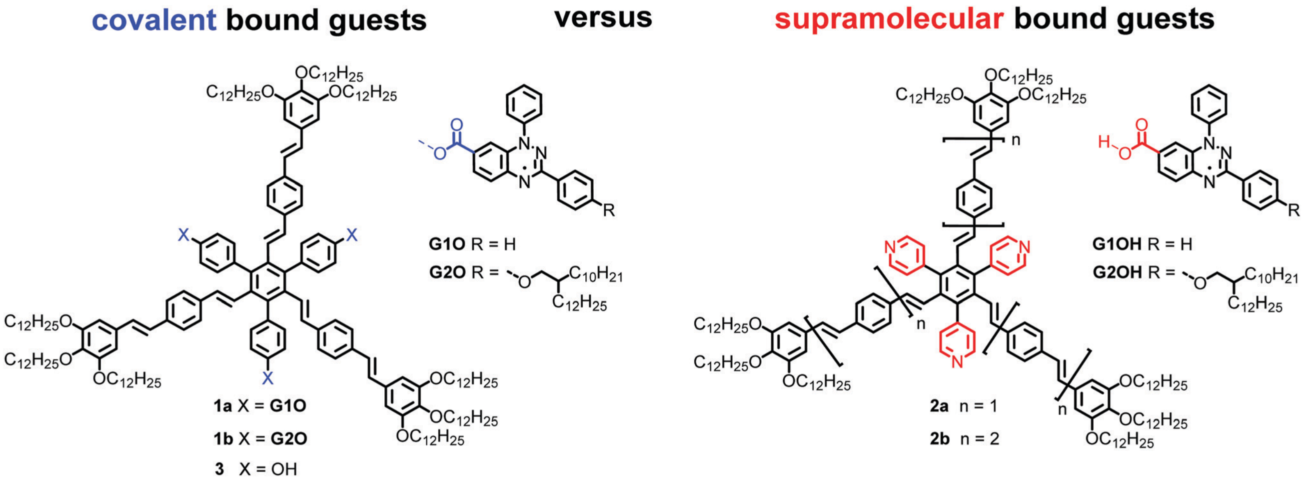

Fig. 1 Structures of radical mesogens **1a** and **1b**, the supramolecular hosts **2a** and **2b** and the radical guests **G1OH** and **G2OH**.

Herein we report on the effect of the covalent *vs.* the supramolecular binding in the cavity of the host mesogen, the impact of the cavity size ($n = 1$ and 2) and the substitution of the Blatter radical on the thermotropic and magnetic behaviour of the material. The comprehensive temperature-dependent structural studies by means of polarized optical microscopy (POM), differential scanning calorimetry (DSC), X-ray scattering (XRS) and polarized FT-IR spectroscopy demonstrated low clearing, enantiotropic columnar soft crystalline and columnar liquid crystalline phases of radical supermesogens in a broad temperature range. The magnetic properties have been explored through solid-state SQUID and EPR measurements showing dissimilar behaviour for covalent and supramolecular bound paramagnetic guests. This new paradigm opens up an attractive direction in the design of tailored paramagnetic soft materials.

Results and discussion

Synthesis

Compounds **1a** and **1b** were obtained by threefold Steglich esterification of triphenol **3** with carboxylic acids **G1OH** and **G2OH**, respectively. Mixtures of star mesogens **2a** and **2b** with **G2OH** were prepared in CH_2Cl_2 solutions followed by removal of the solvent and freeze-drying. Mixtures of **2** with acid **G1OH** macroscopically segregated owing to the strong crystallization tendency of the acid and were not considered further.

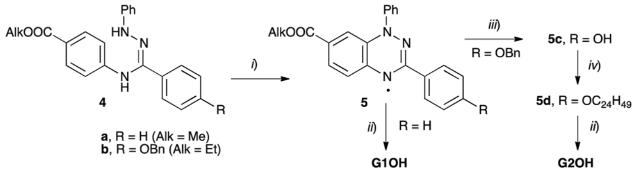

Scheme 1 Synthesis of carboxylic acids **G1OH** and **G2OH**. Reagents and conditions: (i) air, Pd/C, DBU, CH_2Cl_2, rt, overnight; (ii) KOH, THF/MeOH/H_2O, reflux, 8 h; (iii) H_2 (50 psi), Pd/C, EtOH/THF, 16 h; (iv) $C_{24}H_{49}Br$ (**6**), K_2CO_3, DMF.

The synthesis of the carboxylic acids **G1OH** and **G2OH** relied on the classical cyclization of amidrazones,[39] as shown in Scheme 1. Thus, the two carboxylic acids were obtained by aerial oxidation of freshly prepared amidrazones **4a** and **4b** in the presence of Pd and a base to give the esters **5a** (71% yield) and **5b** (86% yield), respectively. The phenolic group in the latter ester was deprotected under reductive conditions (H_2/Pd) and the resulting phenol **5c** was alkylated with 2-decyltetradecyl bromide (**6**) to give the ethyl ester **5d**. Both esters, **5a** and **5d**, were hydrolyzed with KOH in a MeOH/THF/H_2O mixture giving acids **G1OH** and **G2OH** in 43% and 40% overall yield, respectively.

The requisite amidrazone **4a** was prepared in 52% yield by reaction of hydrazonoyl chloride[40] **7** with methyl 4-aminobenzoate (Scheme 2). A similar reaction with the 4-benzyloxy analogue of chloride **7** did not yield the desired amidrazone **4b**. Instead, the requisite amidrazone was obtained in 24% yield by reacting phenylhydrazine with benzimidoyl chloride **8** (Scheme 2). The chloride **8** was prepared from amide **9** in reaction with $SOCl_2$ (Scheme 3). Mesogens **2** and the tri-hydroxyphenyl mesogen **3** (Fig. 1) were prepared according to literature procedures.[33,38,41]

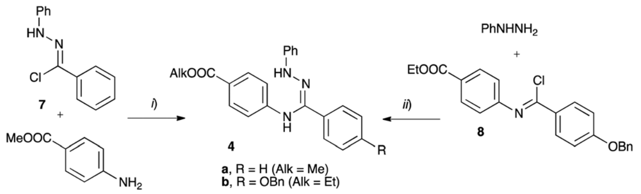

Scheme 2 Synthesis of amidrazone **4**. Reagents and conditions: (i) EtOH, Et_3N, reflux, 2 h; (ii) Et_3N, CH_2Cl_2, rt, overnight.

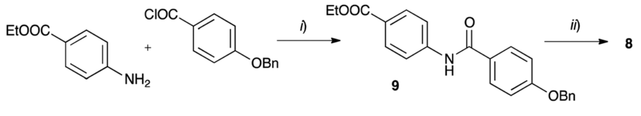

Scheme 3 Synthesis of benzimidoyl chloride **8**. Reagents and conditions: (i) Et_3N, CH_2Cl_2, rt, overnight: (ii) $SOCl_2$, reflux, 24 h.

Thermotropic properties: POM and DSC studies.

The thermotropic properties of all LC materials were studied by POM and DSC methods. The results are summarized in Table 1 and shown in Fig. 2. The supermesogens **1a** and **1b** do not reveal any transition to the isotropic phase below 300 °C, consequently, no characteristic LC textures could be obtained from POM observations. Nevertheless, the materials are birefringent under crossed polarizers and can be planar aligned by shearing, demonstrating the LC character of the samples. The supermesogen planes are on average oriented orthogonal to the column direction, which is concluded from the blue colour of the textures (Fig. 2(B) and (D)) originating from the addition of the largest refractive index of the sample and the largest index of the λ-compensation plate inserted perpendicular to the shearing direction and the complete extinction of light when one of the polarizers is parallel to the shearing direction (not shown). Both substances exhibit a reversible transition from a low temperature viscous, highly ordered, soft crystalline phase ($\mathrm{Cr_{soft}}$) for **1a** and an oblique columnar phase ($\mathrm{Col_{ob}}$) for **1b** to more fluid hexagonal columnar phases at 117 °C (**1a**) and at 114 °C (**1b**), respectively. The transition to the LC state is accompanied by an increase in birefringence.

The LC properties of the pure hosts **2a** and **2b** were already reported, and it was concluded that their molecules arrange in hexagonal double helical columnar phases ($\mathrm{Col_{hH}}$).[33,38] The clearing temperatures increase with the length of the conjugated arm from 138 °C for **2a** (n = 1) to 194 °C for **2b** (n = 2).

The existence of mesophases in the presence of the guests **G1OH** and **G2OH** was initially investigated with contact samples for **2a** and **2b** in POM.[42] Mixing of **2a** with **G1OH** results only in macroscopic phase separation, owing to the stable crystal phase of **G1OH**, with a melting point >300 °C. In contrast, the guest **G2OH** with the branched peripheral chains possesses a much lower melting temperature (168 °C), which allows the formation of stable hydrogen bonded supermesogens with both hosts **2a** and **2b** and the self-assembly in new functional mesophases. Subsequently, for both hosts mixtures with radical **G2OH** (**2a-G2** and **2b-G2**) with an increasing fraction of the radical were prepared (1 : 1, **2a-G2$_1$** and **2b-G2$_1$**; 1 : 2, **2a-G2$_2$** and **2b-G2$_2$**; 1 : 3, **2a-G2$_3$** and **2b-G2$_3$**; Table 1). It was rationalized stochastically that 1 : 1 and 1 : 2 systems consist of equilibrium mixtures of different complexes with the 1 : 1 and 1 : 2 complexes, respectively, being the major components. Only for the fully filled cavities (the 1 : 3 system) is the material nearly completely composed of the 1 : 3 supermesogens.[38] Interestingly, the clearing transitions (DSC, heating rate 10 K min^{-1}) are well defined with widths of only 4–6 K for the pure hosts and their mixtures. For all mixtures characteristic mosaic textures for columnar phases have been observed (Fig. 2(E) and (F)).[37] In the case of **2a**, the mesophase stability, *i.e.* the clearing temperature, increases with the increasing number of guest molecules. The maximum stability of the LC phase is achieved for the 1 : 3 mixture (**2a-G2$_3$**) with the completely filled cavities.

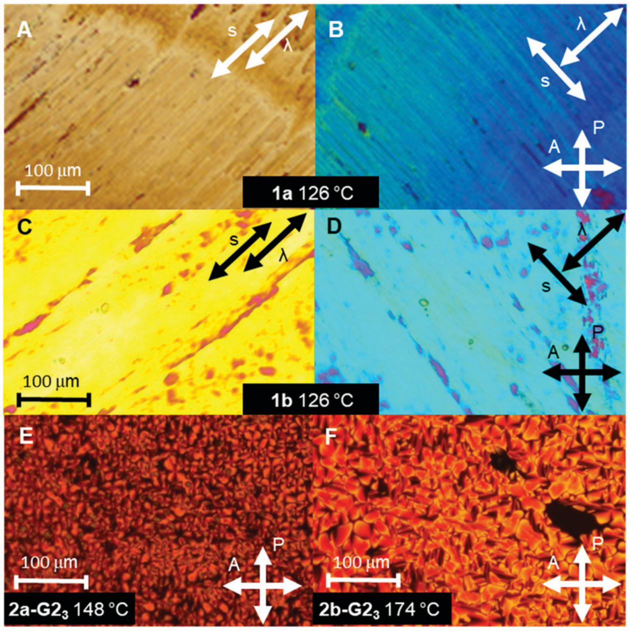

Fig. 2 POM textures under crossed polarizers. Textures of **1a** (A) and (B) and **1b** (C) and (D) after orientation by shearing with the inserted λ-compensation plate. The blue birefringence colour with the λ-plate orthogonal to the shearing direction (B) and (D) indicates that the supermesogens are oriented with their normal of the discs parallel to the column direction. Mosaic textures of 1 : 3 mixtures of **2a** (E) and **2b** (F) with the radical guest **G2OH**.

Table 1 Thermotropic properties of **1** and **2-G2**[a]

Compd	Phase behavior
1a	$\mathrm{Cr_{soft}(Col_{ob})}$ 117 (19.1/48.9) $\mathrm{Col_h}$ > 300 °C (dec.)[b] $\mathrm{Col_h}$ 109 (−19.3/−49.3) $\mathrm{Cr_{Soft}}$ ($\mathrm{Col_{ob}}$)
1b	$\mathrm{Col_{ob}}$ 114 (15.8/40.7) $\mathrm{Col_h}$ > 300 °C (dec.)[b] $\mathrm{Col_h}$ 123 (−16.9/−43.4) $\mathrm{Col_{ob}}$
2a[c]	g($\mathrm{Col_h}$) 89 (T_g) $\mathrm{Col_{hH}}$ 138 (5.7/13.8) I
2a-G2$_1$	$\mathrm{Col_h}$ 145 (7.2/17.2) I[d] I 141 (−4.9/−11.8) $\mathrm{Col_h}$
2a-G2$_2$	$\mathrm{Col_h}$ 152 (11.4/26.7) I[d] I 148 (−7.1/−16.6) $\mathrm{Col_h}$
2a-G2$_3$	$\mathrm{Cr_{soft}(Col_{ob})}$ 67 (58.0/173.1) $\mathrm{Col_h}$ 154 (11.7/27.6) I I 152 (−11.2/−26.2) $\mathrm{Col_h}$
2b[c]	g($\mathrm{Col_{orh}}$) 153 (T_g) $\mathrm{Col_{hH}}$ 194 (9.6/20.5) I
2b-G2$_1$	$\mathrm{Cr_{soft}}$ 81 (20.0/56.3) $\mathrm{Col_h}$ 183 (1.6/3.51) I No visible transition in DSC[e]
2b-G2$_2$	$\mathrm{Col_h}$ 186 (9.2/20.0) I I 182 (−5.1/−11.1) $\mathrm{Col_h}$
2b-G2$_3$	$\mathrm{Cr_{soft}(Col_{ob})}$ 74 (−13.4/−38.6) $\mathrm{Cr_{soft}(Col_{ob})}$ 117 (8.4/21.5) $\mathrm{Col_h}$ 183 (11.8/25.8) I I 179 (−6.8/−14.9) $\mathrm{Col_h}$ 60 (T_g) g ($\mathrm{Col_h}$)

[a] Transition temperature onset (°C) and transition enthalpy (kJ mol^{-1})/transition entropy (J K^{-1} mol^{-1}) in parentheses. First heating and cooling cycles at 10 K min^{-1}: Col columnar LC phase; h hexagonal; hH hexagonal helical; ob oblique; $\mathrm{Cr_{soft}}$ soft crystal; g($\mathrm{Col_h}$) glassy hexagonal columnar phase; g($\mathrm{Col_{orh}}$) glassy orthorhombic columnar phase; T_g glass temperature; I isotropic phase. [b] Compounds decompose at >300 °C, before clearing. [c] Data from ref. 33 and 38. [d] Heating rate 15 K min^{-1}. [e] POM observations of the growing textures at 187 °C.

For this mixture the clearing temperature increases by 15 K to 153 °C relative to that of the pure host. The increase in the clearing temperature is a function of entropy and enthalpy, since at the phase transition $\Delta H = T\Delta S$.

A LC supermesogen, which can dissociate at least partially into a number of building blocks at the transition to the isotropic liquid, exhibits a stronger increase of entropy, when compared with a system in which the mesogen keeps its integrity (*e.g.* covalent mesogens **1**). According to the above equation, it is therefore expected that the clearing temperature decreases with the increasing number of building blocks constituting the supermesogen. On the other hand, the filling of the free space in the supermesogen results in a larger intermolecular interaction surface leading to higher enthalpies. Consequently, the enthalpy increases with an increasing number of H-bonding guests. For **2a** this energy increase overcompensates the entropy change, which results in an increase in the clearing temperatures with increasing number of guests. This finding is in contrast to the previous studies, in which the 1 : 2 mixtures (not 1 : 3) with smaller guests always formed the most stable phase.[38] This was explained by the formation of a completely filled double helix. Contrary to that, the larger π-surface of the guest **G2OH** prevents the formation of helices, presumably owing to stronger intracolumnar interactions. This suggestion is supported by the increasing transition enthalpy from 5.7 kJ mol^{-1} for the pure **2a** to the maximum value of 11.7 kJ mol^{-1} for the 1 : 3 mixture. Eventually, the much-reduced clearing temperature compared with the covalent bonded mesogen **1b** can be explained by the entropy effect.

A different behaviour is observed for the mesophase stabilities of mixtures **2b-G2$_{1-3}$**, which are reduced relative to that of the pure host. Among the supramolecular materials, the 1 : 2 mixture **2b-G2$_2$** shows the highest stability with a clearing transition at 186 °C, thus a reduced stability by 8 K relatively to pure **2b**. In contrast, both the 1 : 1 and the 1 : 3 mixtures exhibit a lower stability with transition temperatures at 183 °C, *i.e.* a reduction of 11 K compared with the pure host. This stability series has also been reproduced by contact samples (see the ESI†). The lower stability of the Col$_h$ phases of all binary materials compared with the pure host is in contrast to the previous findings, in which a longer guest forms materials in 1 : 1 and 1 : 2 ratio with clearing temperatures exceeding that of the pure host.[33] This indicates a mismatch between the pocket size (free space) of the star mesogen **2b** and the size of guest **G2OH** in the present case. The smaller pockets of **2a** suit obviously much better the size of the guests and restrict them to better-defined positions. A comparison of the transition enthalpies and entropies (ΔH and ΔS) of the pure hosts **2a** and **2b** (5.7 kJ mol^{-1}; 13.8 J K^{-1} mol^{-1} and 9.6 kJ mol^{-1}; 20.5 J K^{-1} mol^{-1}) with those for the 1 : 1 mixtures **2a-G2$_1$** and **2b-G2$_1$** (7.2 kJ mol^{-1}; 17.2 J K^{-1} mol^{-1} and 1.6 kJ mol^{-1}; 3.5 J K^{-1} mol^{-1}) demonstrates that the ΔH and ΔS values increase for the mixture of the smaller host and they considerable decrease for the mixture of the larger host **2b**. This indicates a higher order in the mesophases of the smaller supramolecular system, when compared with the larger system, in which the guest has much more space to occupy. The radical guest **G2OH** destabilizes considerably the more ordered helical columnar packing structure of the pure host **2b**, which might be attributed to the mixing of the branched aliphatic chain from the small guest with the aromatic building block (*vide infra*).

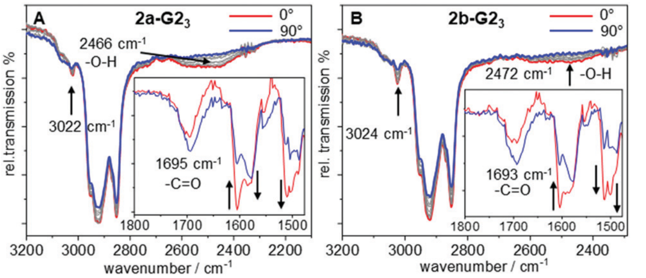

Fig. 3 Polarized FT-IR spectra at room temperature of the 1 : 3 mixtures between **2a** and **G2OH** (A) and **2b** and **G2OH** (B). The arrows indicate the change in intensity of the vibrational bands with a rotating polarizer.

Analysis of the data in Table 1 demonstrates that only mixtures **2a-G2$_3$**, **2b-G2$_1$** and **2b-G2$_3$** reveal crystalline or soft crystalline phases at low temperatures. However, these phases are observed only for pristine samples in the first heating cycle. The hexagonal columnar phases supercool and persist after the first heating. A glass transition has been detected for **2b-G2$_3$** at 60 °C[42] rationalizing this stability of the Col$_h$ phase, however, even annealing above the glass transition for several hours did not recover the soft crystalline phase. Interestingly, after extrusion of fibres from the Col$_h$ phase, the soft crystalline phases can be observed in a subsequent heating cycle by X-ray scattering.[42] This can be rationalized with the frozen high temperature phase, which is not in thermodynamic equilibrium after extrusion and thus the non-optimized packing allows structural reorganization.

FT-IR studies

To gain further insight in the H-bonded structures of supermesogens **2a-G2$_3$** and **2b-G2$_3$**, FT-IR studies have been performed on aligned samples, which were obtained by shearing of the Col$_h$ phase at 130 °C on a KBr plate. The measurements were then performed in the stable Col$_h$ phase at ambient temperature. The polarized FT-IR spectra shown in Fig. 3 demonstrate a broad signal with a maximum at 2466 cm^{-1} for **2a-G2$_3$** and 2472 cm^{-1} for **2b-G2$_3$**, when the polarizer is aligned orthogonal to the column direction. This intensity can be attributed to the H-bond between the carboxylic acid and the pyridyl units. When the polarizer is rotated by 90°, the signal almost completely disappears. Similarly, well-defined absorptions at 3022 cm^{-1}/3024 cm^{-1} for **2a-G2$_3$**/**2b-G2$_3$**, attributed to aromatic CH-stretching vibrations oriented orthogonal to the column axis, also decrease when the polarization direction is changed. Owing to the steric congestion at the central hexa-substituted benzene ring, only peripheral aromatic building blocks of the host allow such an alignment.

Since both stretching vibrations are found predominantly orthogonal to the column direction, this confirms the discotic structure of the supermesogens, with hydrogen-bonded guests in the cavities. These results are consistent with the POM findings. The C═O stretching vibration is found to be the

Table 2 Unit cell parameters, density and molecular volume for **1** and **2-G2**

Compd	Phase	T/°C	a/Å[a]	c[b]	ρ[c]	$V_{m,T}$[d]
1a	Col_h	150	42.5	4.05	0.941	6275
1b	Col_{ob}	25	[f]			
	Col_h	136	47.2[e]	4.25	0.942	8135
2a-G2$_1$	Col_h	110	44.8	3.25[e]		
2a-G2$_2$	Col_h	110	45.5	3.81[e]		
2a-G2$_3$	$Cr_{soft}(Col_{ob})$	66	[f]			
	Col_h	110	46.1	4.35	0.959	8009
2b-G2$_1$	Col_h	110	54.6	2.47[e]		
2b-G2$_2$	Col_h	110	57.9	2.62[e]		
2b-G2$_3$	Cr_{soft1} (Col_{ob})	25	[f]			
	Cr_{soft2} (Col_{ob})	110[g]	[f]			
	Col_h	110[g]	56.8	3.15	0.929	8815

[a] Unit cell parameter a for hexagonal structures. [b] Thickness of a columnar slice calculated for one molecule in the repeat unit ($Z = 1$). [c] Densities at temperatures T estimated on the basis of the experimental densities obtained by the buoyancy method at 22 °C (see the ESI). [d] Molecular volume ($V_{m,T}$) at temperature T. It was assumed that there is only a significant volume change for the aliphatic chains, which was calculated according to the literature.[43] The molecular volume $V_{m,T}$ was calculated as the sum of the molecular volume V_m at 22 °C and the volume change of the aliphatic chains. The density was obtained by $\rho = M/(V_{m,T} \times N_A)$; N_A = Avogadro's constant, M = molecular weight. [e] Estimated thickness based on the density of the 1 : 3 mixture. [f] The oblique columnar structures could not be indexed with high accuracy. A possible indexation with cell parameters (a, b, γ) for the columnar arrangement is given in the ESI. [g] Cr_{soft2} has been measured during first heating, while the data of the Col_h phase has been determined on cooling the sample.

most intense along the column axis, although it still possesses a considerable intensity orthogonal to the column direction. This shows that the orientation of the carboxyl group in the cavity is not well-defined.

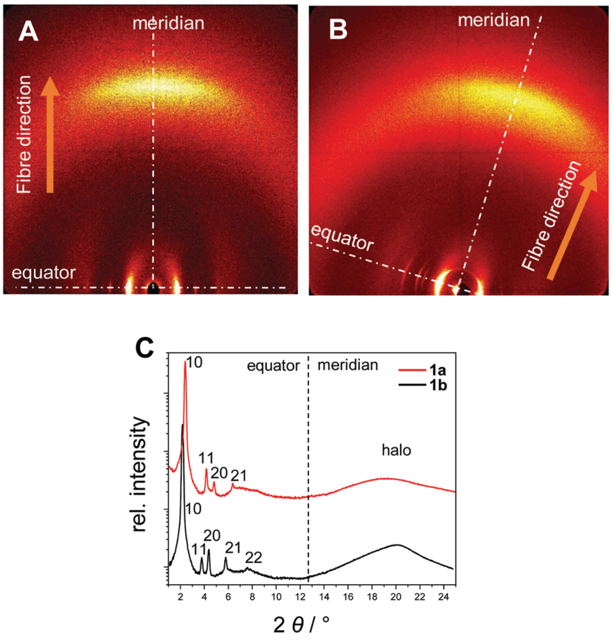

Fig. 4 XRS patterns of the oriented samples in the wide-angle region of **1a** at 150 °C (A) and of **1b** at 136 °C (B). (C) Integration of the diffraction patterns along the equator and the meridian.

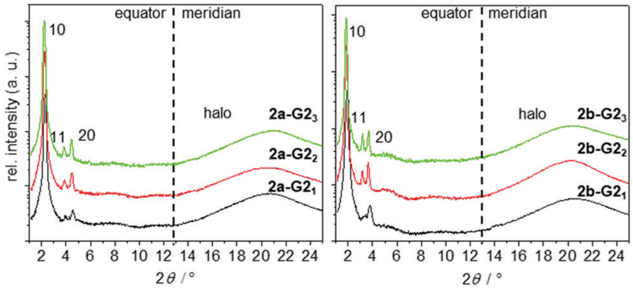

Fig. 5 2θ-scans along the equator and meridian of WAXS patterns of aligned fibres taken in the hexagonal phase at 150 °C of the 1 : 1, 1 : 2, and 1 : 3 mixtures of **2a** and **2b** with **G2**.

XRS investigations

A more detailed picture of the self-assembly of the oligo(phenylenevinylene) scaffolds and the radical building blocks in the LC phases has been established by using XRS techniques. For all temperature-dependent XRS studies, the LC materials were aligned by extrusion to fibres from the respective Col_h phases. The results are shown in Table 2 and Fig. 4–6.

The XRS results for the covalent star mesogens **1a** at 150 °C and **1b** at 136 °C in Fig. 4 show the well-defined equatorial and meridional reflections, which indicate a reasonable good quality of the fibre alignment. The equatorial reflections can be indexed according to a hexagonal columnar phase with a = 42.5 Å (**1a**) and a = 47.2 Å (**1b**). The significant difference in the column diameter can be attributed to the additional branched chains on the radical fragment in **1b**. In the wide-angle region both materials show diffuse signals at 4.7 Å (**1a**) and 4.5 Å (**1b**) with the highest intensity on the meridian. This can be attributed to a superposition of the average distance of liquid-like aliphatic chains and the intracolumnar distance between the disc-like cores. Diffuse intensities are also discerned in the small angle region of **1b**, which indicate a further periodicity along the columns.[42] However, these signals could not be resolved even with SAXS, thus, no further information could be obtained. With the determined density of 0.942 g cm^{-3} for **1b**, a complete molecule fits into a columnar slice of 4.25 Å height, which is in good agreement with the average distance along the column axis (Table 2).

In the case of **1a** the radical fragments possess no aliphatic chains, and consequently the residual free space has to be compensated by the aliphatic chains of the host.[32] At lower temperatures the need for efficient space filling leads to a reversible transition to a lower symmetry oblique columnar soft crystal phase for **1a** and an oblique columnar LC phase for **1b**.

Previous investigation demonstrated that pure hosts **2a** and **2b** arrange in densely packed helical Col_h phases by the formation of discrete propeller-like side-by-side dimers.[33,38] This self-assembly is maintained during the uptake of up to two guests, with the size and shape similar to that of the stilbenoid arms. The third guest transforms the supermesogens to a complete disk and thus the dimer and the helical superstructure is lost. We expected to find similar behaviour in

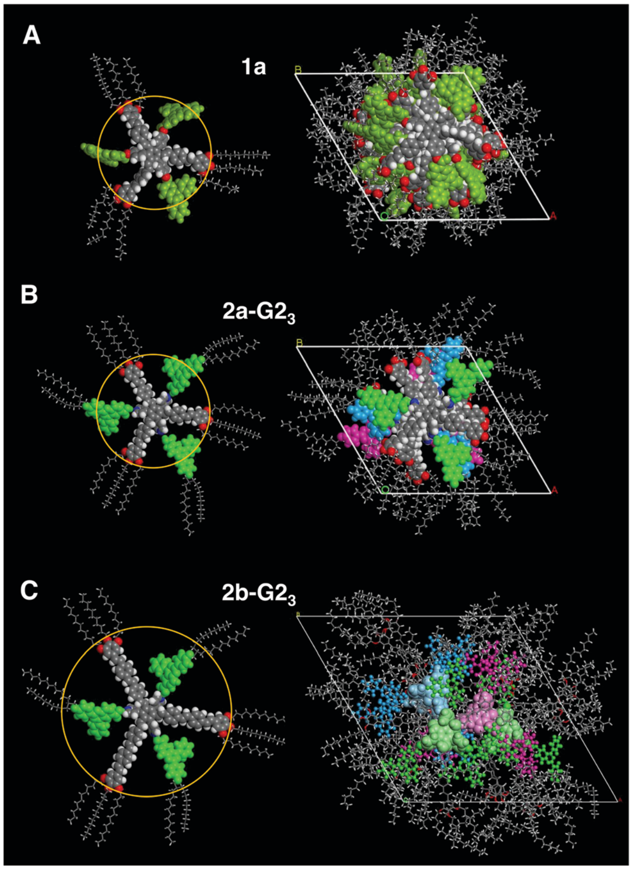

Fig. 6 Left: CPK models of **1a** (A) and the 1 : 3 mixtures of **2a** (B) and **2b** (C) with **G2OH**. The radius of the star mesogens increases from 16.1 Å (**2a**) to 22.2 Å (**2b**). The length of the radical guest **G2OH** is 13.4 Å. Right: Geometry optimized packing models of **1a** (A), **2a-G2$_3$** (B), and **2b-G2$_3$** (C). While the smaller mesogens (A and B) stack essentially on top of each other along the column, the larger supermesogens have to deviate from the centre of the column to enable dense packing structures (for a clearer view of model C the radicals are visualised as sticks and balls, while the conjugated arms are illustrated by a stick representation).

complexes **2-G2**. XRS experiments revealed however, that complexes of the smaller host **2a** give similar XRS patterns at comparable temperatures for all three ratios with guest **G2OH** (1 : 1, **2a-G2$_1$**; 1 : 2, **2a-G$_2$**; 1 : 3, **2a-G2$_3$**; Fig. 5). The integrated signals on the equator can be assigned to Col$_h$ phases. The column diameter slightly increases from 44.8 to 46.1 Å with the increasing number of guests, but is smaller than that for the pure host forming a double helix (46.7 Å).[38] The absence of any diffuse meridional signals indicate that the double helical structure is already disfavoured with the first accepted guest, although the dimer structure seems to be maintained for the 1 : 1 and 1 : 2 mixtures. This is rationalised from the *c* parameters (Table 2), which are calculated to be in the range of 3.3–3.8 Å for one supermolecule within the repeating unit in the column. This small columnar stacking distance is not reasonable for a partially filled sterically crowded core of single hosts with a thickness larger than 4 Å and points to side-by-side dimers as the basic structural units for this columnar self-assembly. The loss of the helical stacking can be attributed to the sterically more demanding Blatter radical guest **G2OH** possessing a lateral phenyl group, which is turned out of the heterocycle and disc planes. This is based on the experimental results and the previous findings[33,38] of the most reasonable model of the phases with less than three guests. Eventually, the radical guests can perfectly fill all three cavities of the host and, as a result, only one mesogen **2a-G2$_3$**, consisting of the star molecule with three hydrogen-bonded radicals does occupy the average distance of 4.4 Å. This hypothesis is supported by molecular modelling, as highlighted in Fig. 6(B). Note that the radicals are slightly larger than the length of the cavity. This results, however, in additional stabilization of the phase, when compared to the phase behaviour of the pure host or hosts with smaller guests, which frequently destabilize the self-assembly.[33,41]

With its larger conjugated arms, the star mesogen **2b** provides longer cavities relative to those in **2a**. This suggests that the steric interactions of the H-bonded radical are not expected to change much, as compared to those in the analogous complexes of the smaller host **2a**. Therefore, it is not surprising, that the 1 : 1 mixture of radical **G2OH** with the host **2b** exhibits equatorial signals corresponding to a Col$_h$ phase. The density ρ and the *c* parameter indicate for this mixture again mesogenic side-by-side dimers, but, according to the XRS patterns,[42] a helical order is absent. Similarly, all data for the 1 : 2 mixture (**2b-G2$_2$**), especially the unreasonable small *c* parameter for one molecule in the columnar repeating unit, point to a Col$_h$ dimer phase over the whole temperature range, while for the 1 : 3 mixture (**2b-G2$_3$**) the data should be in agreement with an ordinary Col$_h$ phase (Table 1, also see the ESI†). Interestingly, although all cavities are filled in the mixture **2b-G2$_3$**, the height of the repeating unit for one mesogen along the column was calculated to be 3.15 Å (110 °C) at the experimental density of 0.929 g cm^{-3}. This value is smaller than a typical π–π separation, which is about 3.2–3.4 Å[44] and much smaller than the thickness of the crowded benzene core (up to 6.6 Å). Therefore, it is reasonable to assume that two molecules occupy the height of 6.3 Å and are not able to stack with their cores on top of each other in the middle of the column. Instead, they must be translationally shifted from the centre. This model is concluded exclusively on the basis of experimental results. In order to gain a better understanding of how such molecules may realise such a stacking in a columnar LC phase, we performed force field geometry optimisation considering all experimental data. A possible geometry optimised model is shown in Fig. 6(C). It demonstrates a higher disorder of the radical fragment in the LC phase. This is in agreement with the XRS results and with the observed small increase of the transition entropy, when compared to that for the pure host **2b** (Table 1). As mentioned above, the 1 : 3 mixtures were investigated in their freeze-dried and extruded samples at 25 °C and 110 °C. The soft crystalline phases were observed in these materials only in the first heating, for which the equatorial reflections could be attributed to an oblique packing of columns (Table 2, also see the ESI†).

Magnetic properties

Magnetic properties of **1a**, **2a-G3$_3$** and **2b-G2$_3$** were investigated with variable temperature EPR spectroscopy and SQUID

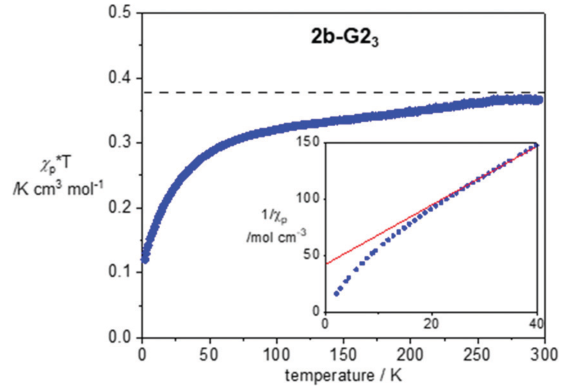

Fig. 7 $\chi_p \times T$ *vs.* T plot for **2b-G2$_3$** in the cooling mode after diamagnetic correction $\chi_{dia} = -0.00559 \times T$ K cm^3 mol^{-1}. For determination of χ_{dia} see the ESI.† The horizontal line marks the Curie constant $C = 0.375$ cm^3 mol^{-1} K. The inset shows the lower portion of the $1/\chi_p$ *vs.* T plot (2–40 K). The red line marks the best-fit line in the range of 30–200 K: $1/\chi_p = 2.684(5) \times T + 42.3(5)$, $r^2 = 0.9998$.

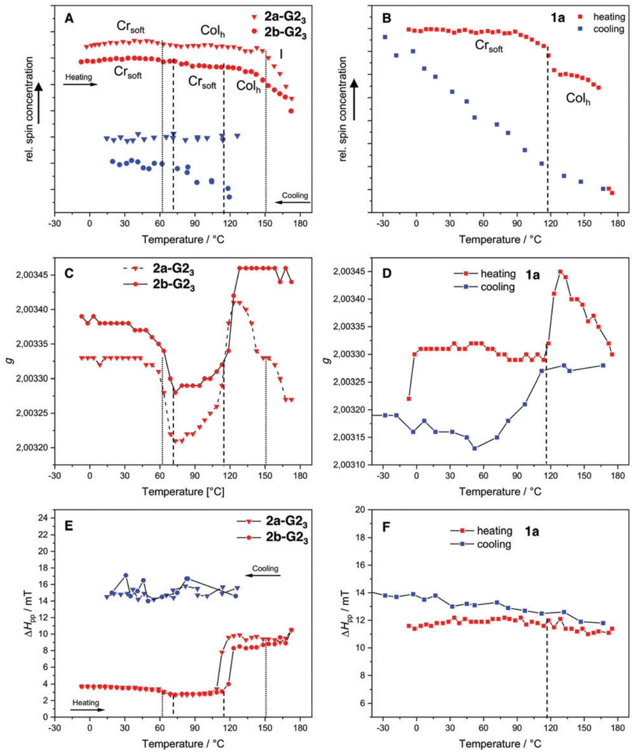

Fig. 8 Temperature dependence of the free spin concentration of the 1 : 3 mixtures of **2a** and **2b** with **G2OH** (A) and **1a** (B) on heating and cooling. The dotted lines highlight the transition temperatures of **2a-G2$_3$** and the dashed lines those of **2b-G2$_3$** and **1a**, respectively. g-Value on heating of **2a-G2$_3$** and **2b-G2$_3$** (C) and g-value of **1a** (D). ΔH_{pp} on heating and cooling of **2a-G2$_3$** and **2b-G2$_3$** (E) and **1a** (F).

magnetometry for neat freeze-dried samples. The former method permitted magnetic characterization of the LC phases in broad temperature ranges. In contrast, limitation of the SQUID magnetometer permitted studies only at lower temperatures, in the solid-state. Magnetic characterization of **2b-G2$_3$** provides an example of such analysis, which was conducted in the temperature range of 300–2 K and magnetic field of 0.6 T for a pristine freeze-dried solid. Analysis of molar paramagnetic susceptibility, χ_p, demonstrated weak antiferromagnetic interactions in the solid state (Fig. 7). The amount of uncompensated spin at 2 K is about 32% and it increases to nearly 100% at 300 K. Curie-Weiss analysis of $1/\chi_p(T)$ plots using eqn (1) revealed a significantly negative Weiss parameter $\theta_W = -16.1$ K for **2b-G2$_3$**.

$$1/\chi_p = (T - \theta_w)/C \qquad (1)$$

It was expected that the covalent system **1a** and the supramolecular systems **2a-G2$_3$** and **2b-G2$_3$** would exhibit different magnetic behavior in the mesophase temperature range accessible by EPR spectroscopy. Therefore, the temperature dependent EPR spectra for the covalent compound **1a** was measured between −30 °C and 180 °C and for the supermesogens **2a-G2$_3$** and **2b-G2$_3$** between −10 °C and 180 °C. The results for relative spin count, which is related to paramagnetic susceptibility χ_p,[45] the gyromagnetic constant g and the peak-to-peak distance ΔH_{pp} are given in Fig. 8. The changing g-values at the phase transitions in LCs indicate reorientations of the material in the magnetic field, while a change in ΔH_{pp} is a function of spin-spin interactions (increasing value with increasing interactions) and spin-exchange interactions (decreasing value with increasing interactions). It is argued that an increase in ΔH_{pp} with a simultaneous decrease of the number of spins (*Ns*) points to an increase of antiferromagnetic interactions.[46]

For the covalent compound **1a** the free spin concentration *N*s undergoes no significant changes on heating until the transition into the Col$_h$ phase at 117 °C, when a steep decrease of 12% is observed (Fig. 8(B), red line). While the ΔH_{pp} is almost constant over the whole temperature range, the change in the g-value indicates that the loss of uncompensated spins can be associated with a reorganisation in the more mobile Col$_h$ phase accompanied by an increase of antiferromagnetic interactions. The cooling cycle (Fig. 8(B), blue line) has nearly linear behaviour with a constant increase of free spins and a slight increase of the ΔH_{pp}. The latter becomes slightly steeper at the phase transition to the soft crystalline phase at 109 °C, at which the decreasing g-value points again to reorganisation of the spin environment (Fig. 8(D)). Therefore, the strength of the antiferromagnetic interactions decreases and, as a consequence, the original number of spins *Ns* is restored. Importantly, it can be noted that the changes in magnetic behaviour for this compound are strongly coupled to the phase transitions.

The EPR curves for **2a-G2$_3$** and **2b-G2$_3$** behave differently, when compared to those of the covalent compound **1a**. Although the LC structures of these two supramolecular materials are evidently distinct, the g-values change similarly at about the same temperatures (50 °C, 115 °C, Fig. 8(C)). After the second change for **2b-G2$_3$** the g-value remains high after the transition to the Col$_h$ phase, while for **2a-G2$_3$** the g-value increases without phase transition starting at 115 °C and falls again starting at 120 °C, even without any phase change. This points to an ongoing reorientation of the paramagnetic units in the increasingly less viscous LC phase. Similarly, the ΔH_{pp} increases at 115 °C (**2a-G2$_3$**) and at 120 °C (**2b-G2$_3$**) pointing to an increase in spin-spin interactions (Fig. 8(E)). This is about 20 K before the *Ns* value decreases more steeply and it seems that these effects are not related to the phase transition (Fig. 8(A)). At higher temperatures the *Ns* falls off for both compounds starting in the range of 140–150 °C. For **2a-G2$_3$** this might be related to the Col$_h$–I phase transition at 153 °C, however, for **2b-G2$_3$** the change starts to take place in the middle of the Col$_h$ phase. This is presumably because, in the disordered and less viscous LC phases of **2b-G2$_3$** the position of the radical guests **G2OH** is not fixed and they can rearrange mutually to optimise their communication, resulting in stronger antiferromagnetic exchange interactions. As the magnetic changes do not clearly coincide with the phase transitions, it appears that the paramagnetic guests in the supramolecular materials rearrange independently from the supermesogens in the LC structures. This clearly points to a more autonomous motion of the hydrogen-bonded paramagnetic building blocks. Upon cooling, supermesogen **2a-G2$_3$** displays a slightly decreasing *Ns* with almost constant spin interactions. These results indicate an increasing order of the discs and antiferromagnetic spin interactions with decreasing temperature. In contrast to **2a-G2$_3$**, *Ns* values increase continuously for **2b-G2$_3$** even though the ΔH_{pp} does not change. These facts may be attributed to the different self-assembly of the supermesogens in the LC phases of **2a-G2$_3$** and **2b-G2$_3$** (Fig. 8(B) and 8(C)). In the LC material **2a-G2$_3$** the radical units are more densely packed with higher order leading, in principle, to stronger spin-spin interactions. In contrast, the supermesogen **2b-G2$_3$** deviates from the centre of the column spatially separating the spin units. This separation persists and may even increase during the slow transformation into the soft crystal, explaining the increasing number of independent spins in the paramagnetic material.

Conclusions

The Blatter radical was successfully incorporated into star-shaped, sterically crowded mesogens either by a covalent link (pseudo-supermesogen) or by supramolecular hydrogen bonding (supermesogen) for the first time. Remarkably, these radicals are so stable that even at high temperatures (up to 250 °C) no decomposition or reactions with the conjugated scaffold are observed. The development of a new radical guest with branched peripheral chains and low melting temperature allowed us to obtain supermesogens self-assembling in enantiotropic columnar mesophases with much lower clearing temperatures than their covalent counterparts. All three cavities of the host materials could be completely filled with the radical units. The size of the cavity was crucial for the self-assembly in the LC phase leading to a more ordered structure for the smaller supermesogen (**2a-G2$_3$**) and a more disordered stacking for the larger (**2b-G2$_3$**) supermesogen, in which the host **2b** provides more free space. EPR studies of the LC materials showed that the magnetic properties are influenced by the cavity size, but also by the method of radical incorporation – covalent vs supramolecular. While for the covalent system the number of uncompensated spins follows the phase transitions, *i.e.* the number of uncompensated spins is lower in the LC phases and increases with the separation of the spin units within the soft crystalline phases, in the supramolecular system the changes are largely independent of the phase transitions. This can be attributed to the mobility of radical units in the cavities of the hosts.

From these perspectives the radical fragments report structural changes within the different soft columnar phases and thus, can be used as spin probes to explore structural details, *e.g.* strength of binding, packing and cavity size, in columnar self-assemblies of shape-persistent supermesogens. With respect to materials science, supermesogens with a combination of low clearing temperatures and paramagnetic Blatter radicals represent a fruitful direction in engineering of paramagnetic soft materials with possibly tuneable magnetic properties.

Experimental section

General

Reagents and solvents were used as received without further purification. If not stated otherwise, reactions were carried out under argon in a flame-dried flask with the addition of the reactants by using a syringe; subsequent manipulations were conducted in air. Dichloromethane was dried over CaH_2 and distilled just before usage. Products were purified by flash chromatography on silica gel (70–200 mesh). Unless stated otherwise, the reported yields refer to analytically pure samples. The melting points were determined using Mel-Temp II apparatus or with a polarising optical microscope and are uncorrected. NMR spectra of non-radical intermediates were recorded with a Bruker AVIII 600 instrument. Chemical shifts are reported relative to solvent residual peaks (^{1}H NMR: δ = 7.26 [$CDCl_3$]; ^{13}C NMR: δ = 77.0 [$CDCl_3$]). All ^{13}C NMR spectra are proton-decoupled. Multiplicity of the ^{13}C NMR signals was assigned using 2D spectra (the HMQC method). IR spectra were recorded with a Cary 630 FTIR spectrometer. ESI-MS spectra were recorded with a Varian 500-MS LC Ion Trap. Mass spectra were recorded on a Bruker-Daltonics *autflex II* (MALDI), on a Bruker-Daltonics *ultrafleXtreme* (HRMS-MALDI), and on a Bruker-Daltonics *micrOTOF focus* and Synapt G2-Si (HRMS-ESI).

The description of other instruments and techniques is provided in the ESI.†

Preparation of compound 1a

Compound **3** (90.0 mg, 34.3 μmol), acid **G1OH** (45.0 mg, 137 μmol), diisopropylcarbodiimide (DIC, 64.1 μL, 51.9 mg, 411 μmol) and 4-(dimethylamino)pyridinium *p*-toluenesulfonate (DPTS, 90.1 mg, 308 μmol) were stirred in a mixture of dried CH_2Cl_2 (40 mL) and dried DMF (10 mL) under nitrogen for 5 days. The reaction mixture was then washed with 1M HCl (3 × 30 mL). The solvent from the organic layer was evaporated under reduced pressure and the crude product was purified by preparative recycling GPC to yield 96.0 mg (269 μmol, 79%) of **1a** as a

Table 3 Amounts for the preparation of mixtures of star mesogen **2** and acid **G2OH**

Mixture	Ratio$_{theo}$[a] **2 : G2OH**	Star mesogen **2**	Acid **G2OH**	Ratio$_{exp}$[b] **2 : G2OH**
2a-G2$_1$	1 : 1 (1.000)	9.98 mg, 3.87 μmol	2.63 mg, 3.87 μmol	1 : 0.999 (1.001 ± 0.005)
2a-G2$_2$	1 : 2 (0.500)	10.00 mg, 3.89 μmol	5.29 mg, 7.77 μmol	1 : 2.005 (0.499 ± 0.001)
2a-G2$_3$	1 : 3 (0.333)	9.96 mg, 3.86 μmol	7.88 mg, 11.60 μmol	1 : 2.999 (0.333 ± 0.001)
2b-G2$_1$	1 : 1 (1.000)	10.10 mg, 3.50 μmol	2.38 mg, 3.50 μmol	1 : 0.999 (1.001 ± 0.005)
2b-G2$_2$	1 : 2 (0.500)	9.99 mg, 3.46 μmol	4.71 mg, 6.92 μmol	1 : 0.999 (0.500 ± 0.002)
2b-G2$_3$	1 : 3 (0.333)	9.98 mg, 3.46 μmol	7.06 mg, 10.40 μmol	1 : 3.000 (0.333 ± 0.001)

[a] Ratio$_{theo}$: theoretical mol ratio $n(\mathbf{2})/n(\mathbf{G2OH})$. [b] Ratio$_{exp}$: experimental mol ratio $n(\mathbf{2})/n(\mathbf{G2OH})$ based on data in columns 3 and 4; the error was calculated based on a weighting error of 0.01 mg.

brownish solid: FT-IR ν 3026, 2919, 2850, 1725, 1577, 1502, 1465, 1428, 1395, 1291, 1226, 1190, 1161 cm^{-1}; EPR g_{iso} = 2.004; a_N = 4.4 G, 4.7 G, and 7.8 G; UV-vis (CHCl$_3$) λ_{max} ($\varepsilon/10^4$) 296 (9.58), 368 (10.52) 518 (0.36) nm; MALDI-HRMS *m*/*z*, calcd for $C_{240}H_{306}N_9O_{15}$: 3554.3453, found: 3554.3585. Anal. calcd for $C_{240}H_{306}N_9O_{15}$: C, 81.04; H, 8.67; N, 3.54; found: C, 80.57; H, 8.74; N, 3.48.

Preparation of compound 1b

Compound **3** (20.0 mg, 7.62 μmol), acid **G2OH** (18.2 mg, 26.6 μmol), diisopropylcarbodiimide (DIC, 14.2 μL, 11.5 mg, 91.3 μmol) and 4-(dimethylamino)pyridinium *p*-toluenesulfonate (DPTS, 22.4 mg, 76.1 μmol) were stirred in a mixture of dried CH_2Cl_2 (20 mL) and dried DMF (7 mL) under nitrogen for 2 days. The reaction mixture was then washed three times with 1 M HCl (30 mL). The solvent from the organic layer was evaporated under reduced pressure and the crude product was purified by preparative recycling GPC to yield 24.0 mg (5.20 μmol, 68%) of **1b** as a dark brown solid: IR ν 2919, 2851, 1725, 1606, 1500, 1465, 1428, 1396, 1225, 1115 cm^{-1}; MALDI-HRMS *m*/*z*, calcd for $C_{312}H_{450}N_9O_{18}$:4611.456, found: 4611.442. Anal. calcd for $C_{312}H_{450}N_9O_{18}$: C, 81.20; H, 9.83; N, 2.73. Found: C, 80.71; H, 10.00; N, 2.87.

Preparation of mixtures 2-G2

Star mesogen **2a** or **2b** (10 mg) and appropriate amounts of acid **G2OH** were dissolved in dry CH_2Cl_2, stirred for 15 min, and the solvent was removed under reduced pressure. Benzene (1 mL) was added and the solution was freeze-dried for 3 h at 1.6×10^{-2} mbar. The resulting spongy material was weighed using a spatula without any rubbing on the flask wall. The stoichiometric data for all mixtures are shown in Table 3.

Preparation of carboxylic acids G1OH and G2OH: General procedure

To a solution of the appropriate ester **5a** or **5d** (0.4 mmol) in THF/H_2O (9 : 1, 6.0 mL) was added methanolic KOH solution (0.1 M, 6.0 mL), and the resulting mixture was refluxed for 8 h. After the mixture was concentrated under reduced pressure to *ca.* 1/5 volume, excess aq. 1% HCl was added, and the crude acid was filtered off. The product was dissolved in a CH_2Cl_2/THF (5 : 1) mixture, washed with several portions of H_2O, the separated organic layer was dried (Na_2SO_4), filtered, and the solvents were removed. The resulting acid **GOH** was recrystallized from the THF/MeCN mixture (3×).

(1,3-Diphenyl-1,4-dihydrobenzo[*e*][1,2,4]triazinyl)-7-carboxylic acid (G1OH)

Brown solid, yield: 80 mg (61%); m.p. 309–313 °C (decomp.); IR (neat) ν 3421, 1680 (C=O), 1432, 1395, 1261 cm^{-1}; ESI-MS (*m*/*z*): 329.1 (47, [M + H]$^+$), 328.1 (100, [M]$^+$), 77 (44). Anal. calcd for $C_{20}H_{14}N_3O_2 \times 0.25H_2O$: C, 72.17; H, 4.39; N, 12.62. Found: C, 72.13; H, 4.29; N, 12.67.

{3-[4-(2-Decyl-1-tetradecyloxy)phenyl]-1-phenyl-1,4-dihydrobenzo[*e*][1,2,4]triazinyl}-7-carboxylic acid (G2OH)

Brown-red solid, yield: 234 mg (86%); m.p. 168–169 °C; IR (neat) ν 2920, 1672 (C=O), 1579, 1394, 1299, 1243, 1165 cm^{-1}; HRMS (ESI-TOF) *m*/*z*, calcd for $C_{44}H_{62}N_3O_3$: 680.4791, found: 680.4805. Anal. calcd for $C_{44}H_{62}N_3O_3$: C, 77.60; H, 9.18; N, 6.17. Found: C, 77.63; H, 9.21; N, 6.15.

Preparation of amidrazone 4a

A mixture of *N*-phenylbenzhydrazonoyl chloride[40] (**7**, 1.15 g, 5.0 mmol), methyl 4-aminobenzoate (0.76 g, 5.0 mmol), and Et_3N (0.61g, 0.84 mL, 6.0 mmol) in EtOH (3.0 mL) was refluxed for 2 h. The solvent was removed under reduced pressure, and the resulting mixture was purified by flash column chromatography (SiO_2, pet. ether/EtOAc 3 : 1) to afford 0.90 g (52% yield) of amidrazone **4a** as a thick yellow oil, which was immediately used for the next cyclisation step: ^{1}H NMR (CDCl$_3$, 600 MHz) δ 3.87 (s, 3H), 6.33 (s$_{br}$, 1H), 6.74 (d, *J* = 8.7 Hz, 2H), 6.88–6.92 (m, 1H), 7.10–7.16 (m, 2H), 7.24–7.29 (m, 2H), 7.35–7.39 (m, 3H), 7.68–7.71 (m, 2H), 7.79 (brs, 1H), 7.91 (d, *J* = 8.7 Hz, 2H).

Preparation of amidrazone 4b

A mixture of amide **9** (2.25 g, 6.0 mmol) and $SOCl_2$ (12 mL) was refluxed for 24 h, and the solvent was removed under reduced pressure to dryness. The resulting yellowish benzimidoyl chloride **8** was dissolved in dry CH_2Cl_2 (30 mL) and Et_3N (0.84 mL, 6.0 mmol) followed by phenylhydrazine (0.60 mL, 6.0 mmol) were added dropwise, and the resulting mixture was stirred at ambient temperature overnight under an inert atmosphere (Ar). The reaction was quenched with excess aq 1% HCl, extracted with CH_2Cl_2 (3 × 15 mL), and the combined organic layers were dried (Na_2SO_4). The solvent was removed and the resulting mixture was flash chromatographed (SiO_2, CH_2Cl_2/EtOAc 4 : 1 gradient to 1 : 1) to give 0.67 g (24% yield) of partially purified amidrazone **4b** isolated as a thick yellow oil, and immediately used for the next step without further handling: ^{1}H NMR (CDCl$_3$, 600 MHz) δ 1.36 (t, J = 7.1 Hz, 3H), 4.33 (q, J = 7.1 Hz, 2H), 5.08 (s, 2H), 5.79 (brs, 1H), 6.69 (d, J = 8.6 Hz, 2H), 6.85–6.89 (m, 1H), 6.95 (d, J = 8.7 Hz, 2H), 7.08–7.12 (m, 3H), 7.24–7.27 (m, 2H), 7.32–7.45 (m, 1H), 7.49 (brs, 1H), 7.63 (d, J = 8.7 Hz, 2H), 7.92 (d, J = 8.6 Hz, 2H).

Preparation of radicals 5a and 5b

To a solution of freshly prepared amidrazone **4** (2.0 mmol) in dry CH_2Cl_2 (5.0 mL) was added 5% Pd/C (85 mg, 8 mol%) followed by DBU (30 μL, 0.20 mmol), and the resulting mixture was stirred overnight at room temperature. The mixture was filtered through Celite, the solvents were removed under reduced pressure, and the resulting material was purified by column chromatography (SiO_2, CH_2Cl_2 gradient 2.5% MeOH in CH_2Cl_2) to yield the desired radical **5**, which was recrystallized from the AcOEt/EtOH mixture.

Methyl (1,3-diphenyl-1,4-dihydrobenzo[*e*][1,2,4]triazinyl)-7-carboxylate (5a)

Black solid, yield: 486 mg (71%); m.p. 241–243 °C (decomp.); IR (neat) ν 1713 (C═O), 1434, 1392, 1300, 1239, 198 cm^{-1}; ESI-MS *m*/*z* 343.2 (100, $[M + H]^+$), 342.2 (71, $[M]^+$). Anal. calcd for $C_{21}H_{16}N_3O_2$: C, 73.67; H, 4.71; N, 12.27. Found: C, 73.63; H, 4.93; N, 12.04.

Ethyl {3-(4-benzyloxyphenyl)-1-phenyl-1,4-dihydrobenzo[*e*][1,2,4]triazinyl}-7-carboxylate (5b)

Black brown solid, yield: 785 mg (85%); m.p. 182–183 °C; IR (neat) ν 1694 (C═O), 1582, 1394, 1230, 1169, 1152, 1012 cm^{-1}; HRMS (ESI-TOF) *m*/*z* calcd for $C_{29}H_{25}N_3O_3$: 463.1896, found: 463.1903. Anal. calcd for $C_{29}H_{24}N_3O_3$: C, 75.31; H, 5.23; N, 9.09. Found: C, 75.30; H, 5.36; N, 9.03.

Preparation of ethyl {3-(4-hydroxyphenyl)-1-phenyl-1,4-dihydrobenzo[*e*]-[1,2,4]triazinyl}-7-carboxylate (5c)

To a suspension of 5% Pd/C (318 mg, 10 mol%) in EtOH (70 mL) a solution of benzyl ether **5b** (693 mg, 1.5 mmol) in THF (54 mL) was added, and the resulting mixture was hydrogenated at 3 atm overnight. The mixture was filtered through Celite and oxidized with air until the yellow leuco form of the phenol **5c** was fully consumed (TLC monitoring). Solvents were removed *in vacuo* (cold bath!), and the crude product was purified by flash column chromatography (SiO_2, CH_2Cl_2 gradient CH_2Cl_2/EtOAc 1 : 1) to yield 391 mg (70%) of **5c** as a back solid: m.p. 215–217 °C; IR (neat) ν 3407 (OH), 1683 (C═O), 1579, 1394, 1239, 1221, 1150, 1129, 1014 cm^{-1}; HRMS (ESI-TOF) *m*/*z*, calcd for $C_{22}H_{19}N_3O_3$: 373.1426, found: 373.1418. Anal. calcd for $C_{22}H_{18}N_3O_3$: C, 70.96; H, 4.87; N, 11.28. Found: C, 71.00; H, 4.99; N, 11.09.

Preparation of ethyl {3-[4-(2-decyl-1-tetradecyloxy)phenyl]-1-phenyl-1,4-dihydrobenzo[*e*][1,2,4]triazinyl}-7-carboxylate (5d)

A mixture of phenol **5c** (223 mg, 0.6 mmol), 2-decyltetradecyl bromide[42] (**6**, 305 mg, 0.73 mmol), solid K_2CO_3 (126 mg, 0.91 mmol), and DMAP (7 mg, 10 mol%) in dry DMF (9 mL) was stirred at 50 °C for 8 h. The resulting mixture was diluted with H_2O (50 mL) and extracted with an Et_2O/EtOAc mixture (1 : 1, 3 × 30 mL). Combined extracts were dried (Na_2SO_4), filtered, and the solvents were removed under reduced pressure. The crude product was purified by column chromatography (CH_2Cl_2/pet. ether 1 : 2 gradient to pure CH_2Cl_2) to yield 332 mg (78%) of **5d** as a brown solid: m.p. 89–90 °C; IR (neat) ν 2920, 2851, 1702 (C═O), 1586, 1394, 1232, 1169, 1027 cm^{-1}; HRMS (ESI-TOF) *m*/*z* calcd for $C_{46}H_{67}N_3O_3$: 709.5182, found: 709.5177. Anal. calcd for $C_{46}H_{66}N_3O_3$: C, 77.92; H, 9.38; N, 5.93. Found: C, 77.90; H, 9.36; N, 5.99.

Preparation ethyl 4-[4-(benzyloxy)benzamido]benzoate (9)

To a solution of 4-benzyloxybenzoic acid (2.28 g, 10.0 mmol) in dry CH_2Cl_2 (23 mL) was added dry DMF (0.12 mL, 1.5 mmol) followed by the dropwise addition of excess oxalyl chloride (1.75 mL, 20.4 mmol) at 0 °C. The mixture was stirred at ambient temperature for 2 h, and the solvents were removed under reduced pressure to dryness. The resulting acid chloride was dissolved in dry CH_2Cl_2 (20 mL), ethyl 4-aminobenzoate (1.65 g, 10.0 mmol) and Et_3N (1.8 mL, 12.9 mmol) were added, and the mixture was stirred at ambient temperature overnight. The reaction was quenched with H_2O (40 mL), extracted with CH_2Cl_2 (3 × 25 mL), combined organic layers were dried (Na_2SO_4) and the solvents were removed *in vacuo*. The resulting crude product was purified by column chromatography (SiO_2, CH_2Cl_2/EtOAc 7 : 1) to afford 3.34 g (89% yield) of amide **9** as a colorless solid: m.p. 203–204 °C; IR (neat) ν 3356, 1707 (C═O), 1657 (C═O), 1605, 1600, 1403, 1277, 1243, 1176, 1098, 1008 cm^{-1}; ^1H NMR ($CDCl_3$, 600 MHz) δ 1.39 (t, J = 7.1 Hz, 3H), 4.37 (q, J = 7.1 Hz, 2H), 5.13 (s, 2H), 7.04 (d, J = 8.8 Hz, 2H), 7.33–7.44 (m, 5H), 7.72 (d, J = 8.7 Hz, 2H), 7.84 (d, J = 8.8 Hz, 2H), 7.98 (brs 1H), 8.04 (d, J = 8.7 Hz, 2H); ^{13}C NMR ($CDCl_3$, 151 MHz) δ 14.3 (q), 60.9 (t), 70.2 (t), 115.0 (d), 119.0 (d), 126.0 (s), 126.9 (s), 127.5 (d), 128.3 (d), 128.7 (d), 129.0 (d), 130.8 (d), 136.2 (s), 142.2 (s), 161.9 (s), 165.1 (s), 166.1 (s); ESI-MS *m*/*z* 398.1 (44, $[M + Na]^+$), 376.1 (100, $[M + H]^+$). Anal. calcd for $C_{23}H_{21}NO_4$: C, 73.58; H, 5.64; N, 3.73. Found: C, 73.61; H, 5.67; N, 3.86.

Author contributions

The manuscript was written through contributions of all authors. All authors have given approval to the final version of the manuscript.

Conflicts of interest

There are no conflicts to declare.

Acknowledgements

Financial support was provided by the German Science Foundation (DFG, LE 1571/5-1) and the National Science Center (NCN, 2017/25/B/ST5/02851). We are especially thankful to Dr Ivo Krummenacher for performing the ESR measurements in solution and to Dr Szymon Kapuściński for his support during the solid-state EPR studies.

References

1 P. A. Heiney, in *Handbook of Liquid Crystals*, eds. J. W. Goodby, P. J. Collings, T. Kato, C. Tschierske, H. Gleeson, P. Raynes and H. F. Gleeson, Wiley-WCH, Weinheim, 2014, vol. 4, pp. 521–567.

2 H. Bock, in *Chirality in Liquid Crystals*, eds. H.-S. Kitzerow and C. Bahr, Springer, New York, 2001, pp. 355–374.

3 T. Kato, J. Uchida, T. Ichikawa and T. Sakamoto, Functional liquid crystals towards the next generation of materials, *Angew. Chem., Int. Ed.*, 2018, **57**, 4355–4371.

4 M. Bremer, P. Kirsch, M. Klasen-Memmer and K. Tarumi, The TV in your pocket: Development of liquid-crystal materials for the new millennium, *Angew. Chem., Int. Ed.*, 2013, **52**, 8880–8896.

5 S. Sergeyev, W. Pisula and Y. H. Geerts, Discotic liquid crystals: A new generation of organic semiconductors, *Chem. Soc. Rev.*, 2007, **36**, 1902–1929.

6 C. V. Garcìa, I. G. Pérez, P. L. Contreras, B. Vinouze and B. Fracasso, in *Optical Switches: Materials and design*, eds. B. Li, S. J. Chua, Woodhead Publishing, 2010, pp. 206–240.

7 Y. Sagara and T. Kato, Stimuli-responsive luminescent liquid crystals: Change of photoluminescent colors triggered by a shear-induced phase transition, *Angew. Chem., Int. Ed.*, 2008, **47**, 5175–5178.

8 M. B. Casu, Nanoscale studies of organic radicals: Surface, interface, and spinterface, *Acc. Chem. Res.*, 2018, **51**, 753–760.

9 M. P. de Jong, Recent progress in organic spintronics, *Open Phys.*, 2016, **14**, 337–353.

10 S. Sanvito, Molecular spintronics, *Chem. Soc. Rev.*, 2011, **40**, 3336–3355.

11 M. Mas-Torrent, N. Crivillers, C. Rovira and J. Veciana, Attaching persistent organic free radicals to surfaces: How and why, *Chem. Rev.*, 2012, **112**, 2506–2527.

12 F. Ciccullo, N. M. Gallagher, O. Geladari, T. Chasse, A. Rajca and M. B. Casu, A derivative of the Blatter radical as a potential metal-free magnet for stable thin films and interfaces, *ACS Appl. Mater. Interfaces*, 2016, **8**, 1805–1812.

13 A. S. Poryvaev, E. Gjuzi, D. M. Polyukhov, F. Hoffmann, M. Froba and M. V. Fedin, Blatter-radical-grafted mesoporous silica as prospective nanoplatform for spin manipulation at ambient conditions, *Angew. Chem., Int. Ed.*, 2021, **60**, 8683–8688.

14 A. S. Poryvaev, D. M. Polyukhov, E. Gjuzi, F. Hoffmann, M. Forba and M. V. Fedin, Radical-doped metal–organic framework: Route to nanoscale defects and magnetostructural functionalities, *Inorg. Chem.*, 2019, **58**, 8471–8479.

15 P. Kaszynski, S. Kapuściński and S. Ciastek-Inskrzycka, Liquid crystalline derivatives of heterocyclic radicals, *Adv. Heterocyc. Chem.*, 2019, **128**, 263–331.

16 R. Tamura, Y. Uchida and K. Suzuki in *Handbook of Liquid Crystals*, eds. J. W. Goodby, P. J. Collings, T. Kato, C. Tschierske, H. F. Gleeson, P. Raynes, Wiley-VCH, Weinheim, 2014, vol. 8, pp. 837–864.

17 S. Castellanos, F. López-Calahorra, E. Brillas, L. Juliá and D. Velasco, All-organic discotic radical with a spin-carrying rigid-core showing intracolumnar interactions and multifunctional properties, *Angew. Chem., Int. Ed.*, 2009, **48**, 6516–6519.

18 K. Bajzíková, M. Kohout, J. Tarábek, J. Svoboda, V. Novotná, J. Vejpravová, D. Pociecha and E. Gorecka, All-organic liquid crystalline radicals with a spin unit in the outer position of a bent-core system, *J. Mater. Chem. C*, 2016, **4**, 11540–11547.

19 F. J.-M. Rogers, P. L. Norcott and M. L. Coote, Recent advances in the chemistry of benzo[*e*][1,2,4]triazinyl radicals, *Org. Biomol. Chem.*, 2020, **18**, 8255–8277.

20 H. M. Blatter and H. Lukaszewski, A new stable free radical, *Tetrahedron Lett.*, 1968, **9**, 2701–2705.

21 I. Ratera and J. Veciana, Playing with organic radicals as building blocks for functional molecular materials, *Chem. Soc. Rev.*, 2012, **41**, 303–349.

22 *Stable radicals: fundamentals and applied aspects of odd-electron compounds*, ed. R. Hicks, Wiley & Sons, 2010.

23 J. Z. Low, G. Kladnik, L. L. Patera, S. Sokolov, G. Lovat, E. Kumarasamy, J. Repp, L. M. Campos, D. Cvetko, A. Morgante and L. Venkataraman, The environment-dependent behavior of the blatter radical at the metal–molecule interface, *Nano Lett.*, 2019, **19**, 2543–2548.

24 F. Bejarano, I. J. Olavarria-Contreras, A. Droghetti, I. Rungger, A. Rudnev, D. Gutiérrez, M. Mas-Torrent, J. Veciana, H. S.-J. van der Zant, C. Rovira, E. Burzurí and N. Crivillers, Robust organic radical molecular junctions using acetylene terminated groups for C–Au bond formation, *J. Am. Chem. Soc.*, 2018, **140**, 1691–1696.

25 F. Ciccullo, A. Calzolari, K. Bader, P. Neugebauer, N. M. Gallagher, A. Rajca, J. van Slageren and M. B. Casu, Interfacing a potential purely organic molecular quantum bit with a real-life surface, *ACS Appl. Mater. Interfaces*, 2019, **11**, 1571–1578.

26 S. Kapuściński, A. Gardias, D. Pociecha, M. Jasiński, J. Szczytko and P. Kaszyński, Magnetic behaviour of bent-core mesogens derived from the 1,4-dihydrobenzo[*e*][1,2,4]triazin-4-yl, *J. Mater. Chem. C*, 2018, **6**, 3079–3088.

27 K. I. Shivakumar, D. Pociecha, J. Szczytko, S. Kapuściński, H. Monobe and P. Kaszyński, Photoconductive bent-core liquid crystalline radicals with a paramagnetic polar switchable phase, *J. Mater. Chem. C*, 2020, **8**, 1083–1088.

28 M. Jasinski, S. Kapuściński and P. Kaszyński, Stability of a columnar liquid crystalline phase in isomeric derivatives of the 1,4-dihydrobenzo[*e*][1,2,4]triazin-4-yl: Conformational effects in the core, *J. Mol. Liq.*, 2019, **277**, 1054–1059.

29 M. Jasinski, J. Szczytko, D. Pociecha, H. Monobe and P. Kaszyński, Substituent-dependent magnetic behavior of discotic benzo[*e*][1,2,4]triazinyls, *J. Am. Chem. Soc.*, 2016, **138**, 9421–9424.

30 M. Jasinski, K. Szymańska, A. Gardias, D. Pociecha, H. Monobe, J. Szczytko and P. Kaszyński, Tuning the magnetic properties of columnar benzo[*e*][1,2,4]triazin-4-yls with the molecular shape, *ChemPhysChem*, 2019, **20**, 636–644.

31 S. Kapuściński, J. Szczytko, D. Pociecha, M. Jasiński and P. Kaszynski, Discs, dumbbells and superdiscs: Molecular

and supermolecular architecture dependent magnetic behavior of mesogenic Blatter radical derivatives, *Mater. Chem. Front.*, 2021, **5**, 6512–6521.
32 M. Lehmann, M. Dechant, M. Lambov and T. Ghosh, Free space in liquid crystals–Molecular design, generation, and usage, *Acc. Chem. Res.*, 2019, **52**, 1653–1664.
33 P. Maier, M. Grüne and M. Lehmann, A star-shaped oligo(phenylenevinylene) liquid crystal host with an anthracene guest–A double nanosegregating supermesogen, *Chem. Eur. J.*, 2017, **23**, 1018–1022.
34 M. Lehmann and M. Hügel, A perfect match: Fullerene guests in star-shaped oligophenylenevinylene mesogens, *Angew. Chem., Int. Ed.*, 2015, **54**, 4110–4114.
35 M. Lambov, N. Hensiek, A. C. Poppler and M. Lehmann, Columnar liquid crystals from star-shaped conjugated mesogens as nano-reservoirs for small acceptors, *ChemPlusChem*, 2020, **85**, 2219–2229.
36 J. M. Lehn, in *Supramolecular Chemistry*, Wiley-VCH, Weinheim, 1995, pp. 81–87.
37 M. Hügel, M. Dechant, N. Scheuring, T. Ghosh and M. Lehmann, Fullerene-filled stilbene stars: The balance between isolated C60 helices and 3D networks in liquid crystal self-assemblies, *Chem. Eur. J.*, 2019, **25**, 3352–3361.
38 M. Lehmann and P. Maier, Shape-persistent, sterically crowded star mesogens: From exceptional columnar dimer stacks to supermesogens, *Angew. Chem., Int. Ed.*, 2015, **54**, 9710–9714.
39 P. A. Koutentis and D. L. Re, Catalytic oxidation of N-phenylamidrazones to 1,3-diphenyl-1,4-dihydro-1,2,4-benzotriazin-4-yls: An improved synthesis of Blatter's radical, *Synthesis*, 2010, 2075–2079.
40 C.-Y. Zhang, X.-H. Liu, B.-L. Wang, S.-H. Wang and Z.-M. Li, Synthesis and antifungal activities of new pyrazole derivatives via 1,3-dipolar cycloaddition reaction, *Chem. Biol. Drug Des.*, 2010, **75**, 489–493.
41 M. Lehmann, P. Maier, M. Grüne and M. Hügel, Crowded star mesogens: Guest-controlled stability of meophases from unconventional liquid crystal molecules, *Chem. Eur. J.*, 2017, **23**, 1060–1068.
42 For details see the ESI†.
43 B. Donnio, B. Heinrich, H. Allouchi, J. Kain, S. Diele, D. Guillon and D. W. Bruce, A generalized model for the molecular arrangement in the columnar mesophases of polycatenar mesogens. Crystal and molecular structure of two hexacatenar mesogens, *J. Am. Chem. Soc.*, 2004, **126**, 15258–15268.
44 M. Mantina, A. C. Chamberlin, R. Valero, C. J. Cramer and D. G. Truhlar, Consistent van der Waals radii for the whole main group, *J. Phys. Chem. A*, 2009, **113**, 5806–5812.
45 G. R. Eaton, S. S. Eaton, D. P. Barr and R. T. Weber, *Quantitative EPR: A Practitioners Guide*, Springer, Vienna, 2010.
46 K. Suzuki, Y. Uchida, R. Tamura, S. Shimono and J. Yamauchi, Observation of positive and negative magneto-LC effects in all-organic nitroxide radical liquid crystals by EPR spectroscopy, *J. Mater. Chem.*, 2012, **22**, 6799–6806.